Spectroscopic Micro Imaging Ellipsometry for Studying Effects of Drug Treatment in Colon Cancer Cells

Yu-Da Chen[1,2,3], Chien-Hsun Wu[4], Hao Yun Hsu[1,5], Mai Ibrahim Khaleel[1,2,3], Yia-Chung Chang[1,5], and Han-Chung Wu[4]

[1] *Research Center for Applied Sciences, Academia Sinica, Taipei, 11529, Taiwan*
[2] *Department of Engineering and System Science, National Tsing Hua University, Hsinchu 30010, Taiwan*
[3] *Nano Science and Technology Program, Taiwan International Graduate Program, Academia Sinica and National Tsing Hua University, Taiwan*
[4] *Institute of Cellular and Organismic Biology, Academia Sinica, Taipei, 11529, Taiwan*
[5] *Graduate Institute of Electronics Engineering, National Taiwan University, Tainan 10617, Taiwan*
Corresponding Author: Yia-Chung Chang

ABSTRACT: This work demonstrates biological applications of spectroscopic micro imaging ellipsometry (MIE). MIE Images of single colon cancer cells were obtained by using a rotating compensator ellipsometer (RCE). The spectra of characteristic parameters (Ψ and $\cos\Delta$) in the visible (with wavelength between 500 nm and 750 nm) and related microscopic images, including $\tan\Psi$, $\sin\Delta$, s- and p-polarized reflectances (Is and Ip) in specular-reflection mode were analyzed. We observed several single colon cancer cells without and with various dosages of drug for 1 hour to gain better understandings of the physical changes of colon cancer cells after drug treatment. The MIE images revealed ripple-like outer diffraction patterns and sharp spikes related to cavity resonance modes or light scattering from nucleus inside single colon cells, which changed significantly after drug treatment.
KEYWORDS: Biological Imaging, Cell Analysis, Drug Treatment, Ellipsometry, Image Analysis, Spectroscopy.

I. INTRODUCTION

System biology is a technique to rebuild morphology or structure of biological objects through knowledge in many fields, including engineering for assembling necessary tools, experimental skills for reliable data acquisition, and theoretical computation for reconstructing actual biological system [1]. Several in-vitro techniques for system biology are well-developed such as optical microscopy by using structured light to observe lily pollen grains [2], scanning electron microscopy (SEM) and transmission electron microscopy (TEM) for analyzing specimens in liquid [3], and atomic force microscopy (AFM) by using a cantilever to detect biological material in water [4]. However, these in-vitro bioimaging methods rely on labeling biological objects with fluorescent agents or other coloring agents or measuring biological samples in a vacuum chamber [1]. Biological cells or bacteria might experience physical changes due to dramatically environmental change or chemical reaction in these invasive measurements.

Cancer imaging techniques are aiming at differentiating potential cancer cells from normal cells in early stage diagnosis of all kinds of cancer diseases [5] such that doctors can be well prepared to help patients get their best treatments on specific problems. Nowadays, doctors in hospitals use commercial in-vivo tools for fast screening of cancer cells such as ultrasound, X-rays, computed tomography (CT), positron emission tomography (PET), and magnetic resonance imaging (MRI) [6]. PET provides high-resolution imaging, but it depends on the half-life of cancer tumors [6,7]. MRI requires desired invasive agents for in-vivo molecule tracking studies [6,8,9]. On the other hand, it was pointed out in literatures that nanoparticles are helpful for enhancing the detection sensitivity. A nano-hybrid liposome coated with amphiphilic hyaluronic acid–ceramide (HACE) was chosen to amplify the contrast in CD44 receptor-overexpressing MRI imaging of breast cancer cells [10]. Au nanorods injected into a mouse can serve as a biomarker to provide surface-enhanced Raman scattering imaging on BT549 breast cancer cells [11]. Researchers also investigated silica-based nanoparticles as delivering agent to detect xenografts of MCF-7 human breast cancer cells with surface modifications in MRI diagnosis [12].

In contrast to invasive measurements which use labeling agents, ellipsometry technique is a non-invasive methodology for thin film characterization and material studies in normal atmosphere environment [13]. Through model fitting of Ψ and Δ spectra, one can determine the refractive index and film thickness of a sample accurately with nm resolution [14]. Even for samples with rough surface, effective-medium theory can be used to evaluate the average thickness and dielectric constant of the film medium [15]. In addition, spectroscopic ellipsometry can be used for real-time monitoring of the fabrication and optimization of

fabrication process via plasma-enhanced chemical vapor deposition (PECVD) in low temperature chamber [16]. Due to its nanoscale sensitivity to film thickness, ellipsometry was also used to analyze optical properties of novel two-dimensional materials such as graphene and MoS2 [17,18].

Microscopic imaging ellipsometry (MIE) is a technique to capture polarization dependent distributions of small objects by ellipsometry. In a typical MIE setup, a charge-coupled device (CCD) is used to detect polarization-dependent reflection of light and record images related to the Ψ and Δ signals, which are related to the magnitude and phase of the ratio of reflectivities (which are complex numbers) for p-polarized light and s-polarized light, respectively. We write $r_p / r_s = |r_p / r_s| e^{i(\Delta_p - \Delta_s)} \equiv \tan\psi\, e^{-i\Delta}$ [19]. Potentials of MIE for biomedical and mechanical applications were illustrated in recent literatures, which include the detection of phage M13KO7 on silicon testing chip by observing the reflectionintensity in grayscale via off-null ellipsometry [20], avian influenza virus (AIV) analysis on microfluidic chip array via both null and off-null ellipsometry and rotating compensator ellipsometry (RCE) to determine concentration distribution for interested area [21], and monitoring electrochemical actuation of a gold microstructure surface via rotating analyzer ellipsometry (RAE) with dichroic sheet analyzer [22]. In this paper, we use a modified Multiskop setup to measure the Ψ and Δ spectra and introduce new imaging analysis to study colorectal carcinoma cells and the effect on single coloncancer cell after drug treatment of 1 hour.

II. EXPERIMENTALDESIGN

2.1 Sample Preparation

Three groups of cell samples with various drug doses were prepared in this study. The first group includes 11 original colon cancer cells on glass substrate. The second group includes 7 colon cancer cells on glass substrate after   liposomal doxorubicin (LD) [23]treatment for 1 hour. The third group includes 10 colon cancer cells on glass substrate after   liposomal doxorubicin (LD) treatment for 1 hour. Then we replaced LD-treated culture fluid with pure culture fluid. Therefore, LD only existed inside colon cancer cells. LD is an anti-cancer medicine doxorubicin in liposome, which is used for chemical treatment on colon cancer patient. These original colon cancer cells were cultured by duplicated colon tissue HCT116 (ATCC® CCL-247™), which is from a male adult patient who got disease called colorectal carcinoma. We used Dulbecco's Modified Eagle's medium (DMEM) added with 10% Fetal bovine serum (FBS) as growth medium to culture original colon cancer cells in commercial Millicell EZ SLIDE 4-well structure (Merck Millipore, Germany) as shown in Fig. 1. Millicell EZ SLIDE 4-well structure was put in a thermal chamber with well-controlled environment where temperature is fixed at 37˚C and CO_2 concentration at 10% for 72 hours during the cell duplication process. After 72 hours of culture, we brought the Millicell EZ SLIDE 4-well structure out to room environment and placed it upside-down for an initial check by a conventional microscope (with light shining from the top) followed by MIE measurements. While the Millicell EZ SLIDE 4-well structure was placed upside-down, most culture fluid leaked out, leaving a thin film of culture fluid beneath the glass slide due to the surface tension. At this moment, only the cells attached beneath the glass slide remain and other floating cells already left.
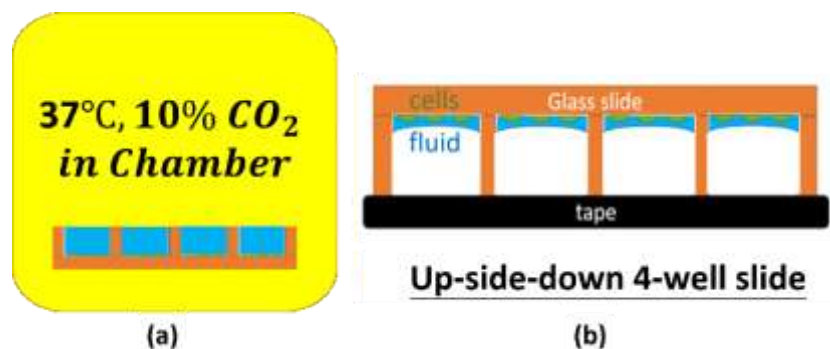

Figure 1. Sample preparation: (a) cell culture in chamber and (b) up-side-down Millicell EZ Slide 4-well structure.

Figure 2 shows the microscopic image taken by 10X conventional bright-field top-illuminating optical microscope. There are single colon cancer cells, multi colon cancer cells, and cell divisions with various shapes. The purple background is caused by the DMEM+10% FBS culture fluid kept beneath the glass slide by surface tension. In this paper, we focus on the study of single fusiform colon cancer cell because it is more stable and better attached to the glass substrate. The size of a fusiform single cancer cell is around 5μm-15μm in diameter.
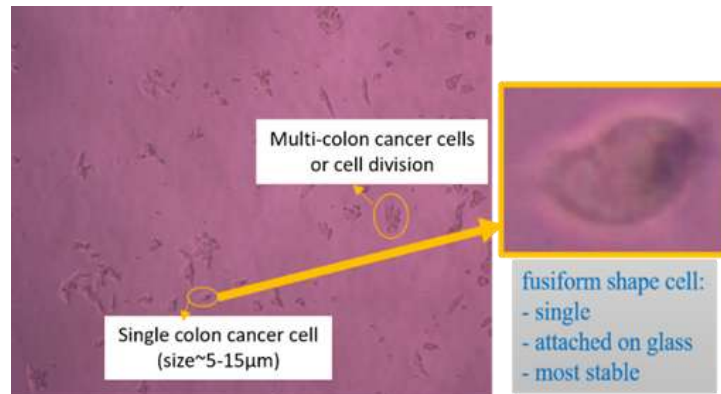
Figure 2. Fusiform shape colon cancer cell by 10X optical microscope.

2.2 Measurement Setup

Our modified Multiskop system (Optrel GbR, Germany) is based on the concept of Rotating-Compensator-Ellipsometry (RCE), as illustrated in Fig. 3. The light source is generated from a supercontinuum fiber laser (Fianium Ltd., United Kingdom) which offers a continuous broadband white light. The broad band laser light is generated in bundled fibers and directed to a monochrometer (Princeton Instruments, USA) for producing single-wavelength light beam via an automatic triple-grating turret and controlled by using LabVIEW (National Instruments Co., USA) software. The selected single-wavelength light beam is then guided into a low-loss fiber connected to the laser arm of the Multiskop system.
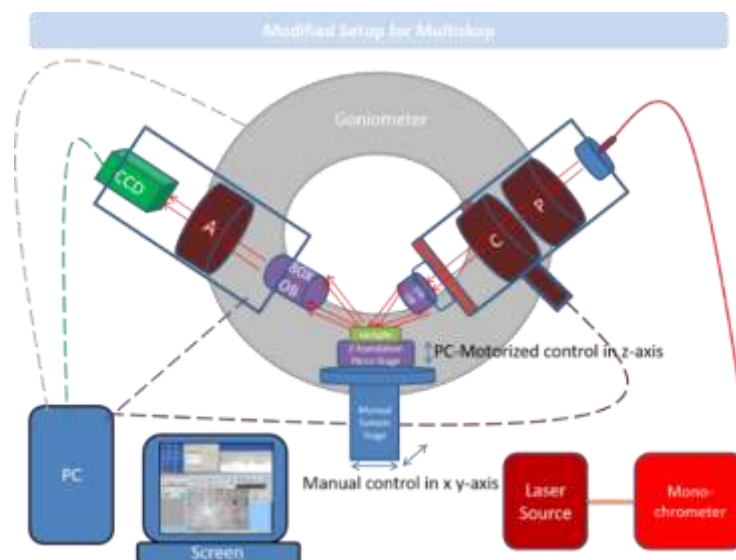
Figure 3. Schematic diagram of modified Multiskop (A is analyzer, C is compensator, and P is polarizer).

A polarizer (Glan-Thompson Polarizing Prism [24], Bernhard Halle Nachfl. GmbH, Germany) is attached to the laser arm, and its orientation is fixed at 45˚ to produce equal strength of s- and p-polarized components of the incident light beam. A motorized compensator is added to the laser arm and monitored by a goniometer. It rotates periodically with the range of angles controlled by a LabVIEW program. The range of rotating angle in our MIE measurements is typically from 5˚ to 175˚ with 10˚ steps. The compensator used is a quarter-wave plate which brings elliptical polarized light with a wavelength-dependent phase delay between the p- and s-polarized light. The elliptically polarized light is then focused onto the sample via a 10X infinity corrected objective (Mitutoyo Co., Japan). The spot size of this focused beam is around 100μm on the sample.

The reflected or scattered light is collected via an 80X long working distance infinity corrected objective (Mitutoyo) with numerical aperture 0.5 attached to the detector arm and captured by a CCD camera (pixelfly qe, PCO AG, Germany) with 2/3" sensor after the light passes through an analyzer. The field of view is 0.11mm✕0.08mm. The orientation of the analyzer (with the same specs as the polarizer) is fixed at 45˚. The output electronic signals picked up by the CCD are transferred and stored in a personal computer (PC) for off-line analysis of the MIE images. Both the laser arm and detector arm are allowed to rotate from 0˚ to 120˚ with

0° corresponding to the direction perpendicular to the sample plane. A goniometer is used for programmable control of the motion of laser arm and detector arm.

Our sample is placed on a motorized z-translation piezo stage (Physik Instrumente GmbH & Co. KG, Germany) which is controlled by LabVIEW program with 10nm spatial resolution in z-direction for fine adjustment. The motorized z-translation piezo stage is fixed on a manual stage with one coarse adjustment control for z-translation in 1mm spatial resolution and two fine adjustment controls for x- and y-translation in 10μm steps. The fine resolution in z-direction is useful for fine tuning of the focal plane relative to the sample surface.

The time to acquire a single image with each designated compensator angle (from 5° to 175° with 10° steps) is about 2s. Thence, the time to get a set of images with single wavelength is about 1min, and the time to obtain a set of spectra (wavelength from 500nm to 750nm with 10nm steps) is about 26min.

Our modified Multiskop MIE setup can be used to measure the difference (both in amplitude and phase) between the p- and s-polarized light after reflection or scattering with pixel size of 82nm. To reduce statistical error, we combine every 2⅟2 grids to form a pixel of 164nm⅟164nm, which gives more stable signal and less noisy MIE images. This allows clear observation of diffraction fringes of scattered light from micro objects in the visible range. The key enabling technique is the adoption of RCE approach instead of the original setup based on null measurement. In the null measurement, both polarizer and analyzer are rotated continuously until the null condition is reached, and the Ψ and Δ parameters can be related to the angles of polarizer and analyzer, which satisfy the null condition. This procedure, however, is time-consuming and the image is blurry due to the fact that image tends to shift more than a few μm as the analyzer rotates (an undesirable feature of the Glan-Thompson prism [23] used) which leads to poor resolution for the image.

2.3 Data Processing Based on Jones' Matrices and Fourier Analysis

The output data from MIE measurements can be converted to characteristic parameters with well-defined physical meanings after suitable analysis. According to the Jones' matrix formulation, the relationship between output and input electromagnetic fields can be described as matrix products related to the functionality of all the optical components, including the polarizer, compensator, and analyzer, as given below [25].

$$J(\phi_A,\phi_C,\phi_P) = \begin{bmatrix} 1 & 0 \\ 0 & 0 \end{bmatrix}\begin{bmatrix} \cos\phi_A & \sin\phi_A \\ -\sin\phi_A & \cos\phi_A \end{bmatrix}\begin{bmatrix} r_s & 0 \\ 0 & r_p \end{bmatrix}\begin{bmatrix} \cos(-\phi_C) & \sin(-\phi_C) \\ -\sin(-\phi_C) & \cos(-\phi_C) \end{bmatrix}\begin{bmatrix} 1 & 0 \\ 0 & e^{-i\delta} \end{bmatrix}\begin{bmatrix} \cos\phi_C & \sin\phi_C \\ -\sin\phi_C & \cos\phi_C \end{bmatrix}\begin{bmatrix} \cos(-\phi_P) & \sin(-\phi_P) \\ -\sin(-\phi_P) & \cos(-\phi_P) \end{bmatrix}\begin{bmatrix} 1 & 0 \\ 0 & 1 \end{bmatrix}\begin{bmatrix} 1 \\ 0 \end{bmatrix}. \tag{1}$$

where $J(\phi_A,\phi_C,\phi_P)$ is the output electromagnetic field. ϕ_A, ϕ_C, ϕ_P are the angles of analyzer, compensator, and polarizer, respectively. r_s, r_p are reflectivities for s- and p-polarized light, respectively. δ represents the phase retardation produced by the compensator. The output intensity $I(\phi_C)$ is the square of output electromagnetic field $J(\phi_A,\phi_C,\phi_P)$, and we obtain :

$$I(\phi_C) = |J(\phi_C)|^2$$
$$= \frac{1}{4}[e^{i\delta}(\cos\phi_C + \sin\phi_C)(r_s\cos\phi_C + r_p\sin\phi_C) + (\sin\phi_C - \cos\phi_C)(r_p\cos\phi_C + r_s\sin\phi_C)]$$
$$\times e^{-i\delta}[(\cos\phi_C + \sin\phi_C)(r_s^*\cos\phi_C + r_p^*\sin\phi_C) + e^{i\delta}(\cos\phi_C - \sin\phi_C)(r_p^*\cos\phi_C - r_s^*\sin\phi_C)]. \tag{2}$$

where r_s^* and r_p^* are complex conjugates of r_s and r_p, respectively. Equation (2) shows that $I(\phi_C)$ takes the following form in terms of polynomials of $\cos(\phi_C)$ and $\sin(\phi_C)$:

$$I(\phi_C) = A_0 + A_2\cos(2\phi_C) + B_2\sin(2\phi_C) + A_4\cos(4\phi_C) + B_4\sin(4\phi_C) \tag{3}$$

By rearranging terms in Eq. (2) and comparing with Eq. (3), we obtain the following relations between Fourier coefficients (A_0, A_2, B_2, A_4, B_4) and (r_S, r_P, δ).

$$A_0 = \frac{1}{8}[r_s^*(r_p + 2r_s + r_p\cos\delta) + r_p^*(2r_p + r_s + r_s\cos\delta)].$$

$$A_2 = \frac{i}{4}\sin\delta(r_s r_p^* - r_p r_s^*).$$

$$B_2 = 0. \tag{4}$$

$$A_4 = \frac{1}{8}(r_s r_p^* + r_p r_s^*)(-1 + \cos\delta).$$

$$B_4 = \frac{1}{8}(|r_p|^2 - |r_s|^2)(-1 + \cos\delta).$$

where A_0 is the DC coefficient. A_2, B_2, A_4, B_4 are AC coefficients for $\cos(2\phi_C)$, $\sin(2\phi_C)$, $\cos(4\phi_C)$, $\sin(4\phi_C)$, respectively. Using the inverse Fourier transform of Eq. (3), we have

$$A_0 = \frac{1}{\pi}\int_0^\pi d\phi_C I(\phi_C) = \frac{1}{18}\sum_{\phi_C=5°,15°,\cdots}^{175°} I(\phi_C)$$

$$A_2 = \frac{2}{\pi}\int_0^\pi d\phi_C I(\phi_C)\cos(2\phi_C) = \frac{1}{9}\sum_{\phi_C=5°,15°,\cdots}^{175°} I(\phi_C)\cos(2\phi_C)$$

$$B_2 = \frac{2}{\pi}\int_0^\pi d\phi_C I(\phi_C)\sin(2\phi_C) = \frac{1}{9}\sum_{\phi_C=5°,15°,\cdots}^{175°} I(\phi_C)\sin(2\phi_C)$$

$$A_4 = \frac{2}{\pi}\int_0^\pi d\phi_C I(\phi_C)\cos(4\phi_C) = \frac{1}{9}\sum_{\phi_C=5°,15°,\cdots}^{175°} I(\phi_C)\cos(4\phi_C)$$

$$B_4 = \frac{2}{\pi}\int_0^\pi d\phi_C I(\phi_C)\sin(4\phi_C) = \frac{1}{9}\sum_{\phi_C=5°,15°,\cdots}^{175°} I(\phi_C)\sin(4\phi_C) \quad \textbf{(5)}$$

In the above, we have replaced the continuous integrals by discrete sums with mid-point approximation. The values on these mesh points correspond to our measured MIE data.

The following relations are used to define Ψ and Δ.

$$\begin{cases} r_p = \rho e^{-i\Delta}\sin\Psi \\ r_s = \rho\cos\Psi \end{cases}, \text{ and } \frac{r_p}{r_s} = \tan\Psi e^{-i\Delta} \textbf{ (6)}$$

Thus, Eq. (4) becomes

$$A_0 = \frac{|\rho|^2}{8}[2-(1-\cos\delta)\sin(2\Psi)].$$

$$A_2 = -\frac{|\rho|^2}{4}\sin\delta\sin\Delta\sin(2\Psi). \qquad \textbf{(7)}$$

$$B_2 = 0.$$

$$A_4 = -\frac{|\rho|^2}{8}(1-\cos\delta)\cos\Delta\sin(2\Psi).$$

$$B_4 = \frac{|\rho|^2}{8}(1-\cos\delta)\cos(2\Psi).$$

Equation (7) becomes simpler for the scaled parameters (A'_2, A'_4, B'_4, A'_{24}) defined as

$$A'_2 = \frac{4A_2}{\sin\delta} = -|\rho|^2\sin\Delta\sin(2\Psi) = -2|r_s r_p|\sin\Delta$$

$$A'_4 = \frac{8A_4}{(1-\cos\delta)} = -|\rho|^2\cos\Delta\sin(2\Psi) = -2|r_s r_p|\cos\Delta \qquad \textbf{(8)}$$

$$B'_4 = \frac{8B_4}{(1-\cos\delta)} = |\rho|^2\cos(2\Psi) = |r_s^2| - |r_p^2|$$

$$A'_{24} = \sqrt{(A'_2)^2 + (A'_4)^2} = |\rho|^2\sin(2\Psi) = 2|r_s r_p|$$

with

$$|\rho|^2 = \sqrt{(A'_{24})^2 + (B'_4)^2} = |r_s^2| + |r_p^2| \textbf{ (9)}$$

$I_S = |r_S|^2$ (s-polarized reflectance), $I_P = |r_P|^2$ (p-polarized reflectance), Δ, and Ψ are then calculated by the following equations.

$$I_S = |r_S|^2 = \frac{(|\rho|^2 + B'_4)}{2} : \text{Reflectance for s-polarized light}$$

$$I_P = |r_P|^2 = \frac{(|\rho|^2 - B'_4)}{2} : \text{Reflectance for p-polarized light} \qquad \textbf{(10)}$$

$$\Delta = \cos^{-1}\left(-\frac{A'_4}{A'_{24}}\right) : \text{Phase difference between p- and s-reflectivities}$$

$$\Psi = \tan^{-1}\left(\frac{|r_P|}{|r_S|}\right) = \tan^{-1}\left(\sqrt{\frac{|\rho|^2 - B'_4}{|\rho|^2 + B'_4}}\right)$$

Since the inverse cosine is defined in the range of $(0, 180°)$, we need to use this value of $\sin \Delta = -A'_2 / A'_{24}$ to determine the sign of Δ. Due to the possible jump of $360°$ in certain areas of the Δ image (as the Δ value is not unique), the Δ image can have artificially large fluctuations. For this reason, the following quantities [$\tan \Psi, \sin \Delta, I_S, I_P$] are chosen in the presentation of MIE images. All these parameters have clear physical meanings as defined in Eq. (10).

III. EXPERIMENTAL RESULTSANDANALYSIS

In this work, MIE images within a 15μm✕15μm area in specular reflection mode were recored. The angles of incidence (AOI) used is 60°. The direct microscopic images (images taken without rotating the compensator) for eleven original colon cancer cells and seventeen LD drug treated cancer cells under study are shown in Fig. 4. We can divide these cells into three groups. The first group consists of original colon cancer cells (labelled 1-11). The second group (cells 12-18) and third group (cells 19-28) consist of colon cancer cells treated with $10 \mu l / g$ and $50 \mu l / g$ LD medicine for 1 hour, respectively.

(a) *Original cells* (cell1-cell11)
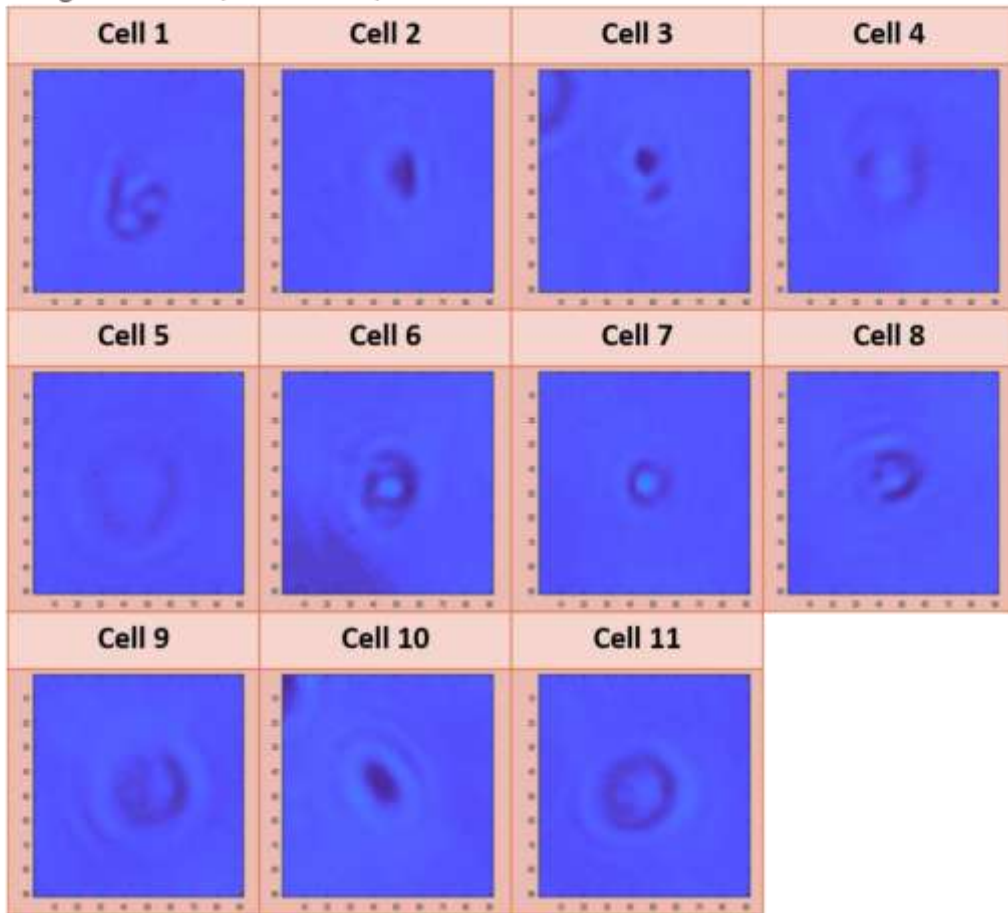
(b) $10\mu l/g$ *LD treated cells* (cell12-cell18)
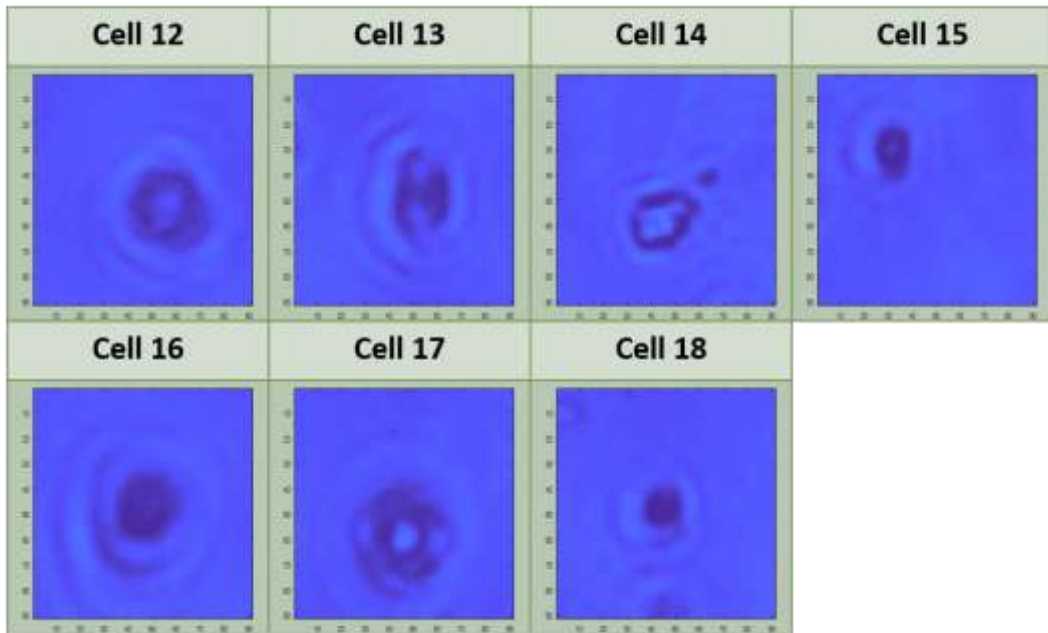
(c) $50\mu l/g$ *LD treated cells*

$group - c1\ (cell19 - cell23)$
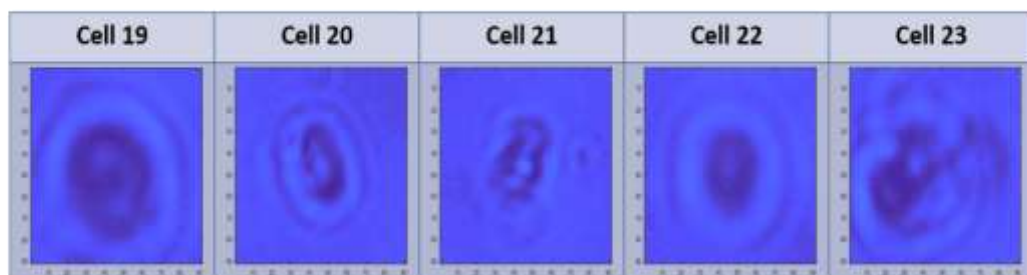
$group - c2\ (cell24 - cell28)$
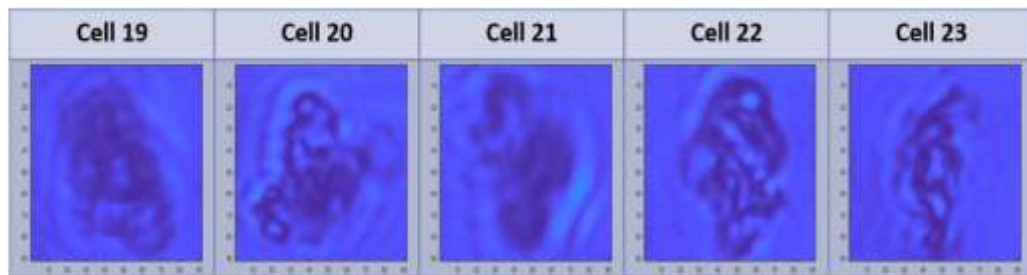
Figure 4. Microscopic images of (a) original colon cancer cells (cells 1-11) (b) $10\mu l/g$ LD treated colon cancer cells (cells 12-18) (c) $50\mu l/g$ LD treated colon cancer cells (group-c1: cells 19-23, group-c2: cells 24-28) when from LabVIEW's display in Multiskop system.

3.1 Ψ and Δ Spectra

As a calibration, we first took MIE spectra for Ψ and $\cos\Delta$ of an empty up-side-down Millicell EZ Slide 4-well structure and compare them withellipsometric spectra obtained bythe V-VASE setup (J.A. Woollam Co., United States, as shown in Fig. 5. Both ellipsometric spectra obtained by MIE and V-VASE shows fast oscillations, which are attributedto the interference effect of light bouncing between the two surfaces of the glass slide. This effect is stronger in MIE measurements since the thickness of slide vary only slightly over the micron-scale area sampled by MIE, while the thickness will vary more over a cm-scale as sampled by VASE. When results for various thicknesses are averaged, the large oscillations in spectra can be reduced.
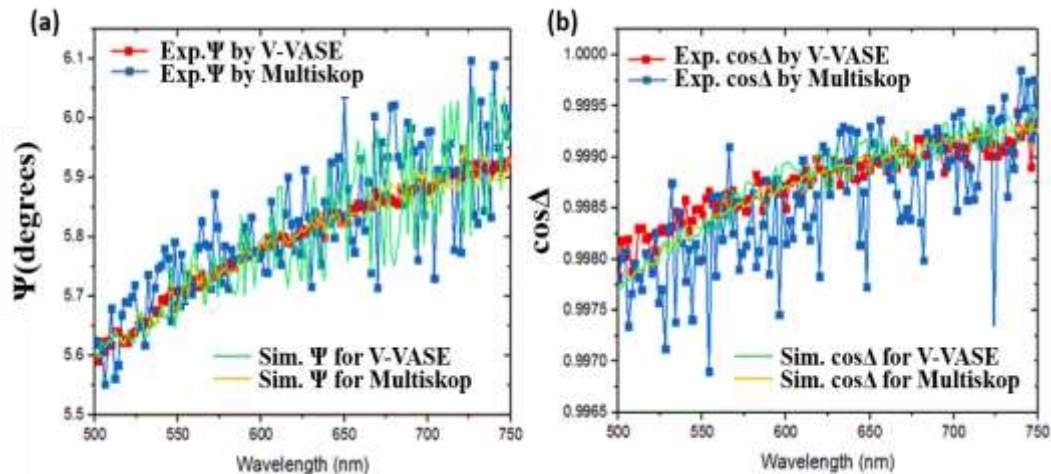
Figure 5. Comparison of experimental and simulated ellipsometric spectra for (a)Ψand (b) cosΔ of Millicell EZ Slide 4-well structure. AOI=60˚.

To understand the fast oscillation, we did a simulation for light reflection from a glass slide with non-uniform thickness.In the simulation we have taken the average of reflectivities obtained for 50 different thickness of the glass slide covering the range of 1mm ±200nm (1mm ± 1μm) for MIE (VASE) measurements. In Fig. 5, it is clear that our simulated curves can fit experimental curves well and show qualitatively similar oscillations. From the simulation, it becomes clear how the fast oscillations due to interference effect can be reduced by the averaging process associated with non-uniform thickness. The wider range of thickness variation significantly reduces the beating oscillation as seen in the VASE measurements and the corresponding simulation. The refractive index (n_1) obtained by fitting is around 1.5 and the extinction coefficient (k_1) varies linearlyfrom 2×10^{-5} (at λ=500nm) to 5.75×10^{-5} (at λ=750nm) for Millicell EZ Slide.

Figure6 shows Ψ and cosΔ spectra for the three groups of colon cancers cells considered. We notice that both Ψ and $\cos\Delta$ spectra oscillate as a result of the interference effect due to light bouncing between glass surfaces. The oscillation in Ψ spectra is comparable to that for Millicell EZ Slide, while the cosΔ shows larger oscillation due to the presence of cells, sinceΔ is more sensitive to the morphology of embedded features. When we take average of ellipsometric spectra of cells within the same group, the fluctuation tends to be averaged out. The resulting spectra become much smoother as shown in Fig. 6(c,d).

For the first group (which includes original single colon cancer cells 1 to 11 as shownin Fig. 4), the average value of Ψ increases from 6.2˚ to 6.6˚ as the wavelength varies from 500nm to 750nm, while the average $\cos\Delta$ is nearly constant with a value around 0.975. The small difference between results for different cells can be attributed to the difference in size and morphology of cells.

For the single colon cancer cells treated with $10 \mu l / g$ LD medicine for 1 hour (which includes cells 12-18 as shown in Fig. 4)the average Ψ spectra increases from 6.1˚ to 6.5˚ as the wavelength changes from 500 nm to 750 nm, while the average value of $\cos\Delta$ are around 0.93. The increased fluctuations in $\cos\Delta$ spectra of these 7 cells are attributed to light scattering from deformed cells with shape deformation varying from cell to cell. Ψ spectra are similar to those of the first group (original single colon cells) but $\cos\Delta$ spectra are clearly different from those of the first group, indicating that drug treatment didn't affect much inside cells but apparently changed the morphology of cells.

For the single colon cancer cells treated with $50 \mu l / g$ LD medicine, we can further divide them into two subgroups (group-c1 and group-c2 in Fig.4).The average Ψ spectra of group-c1 (including cells 19-23) increases from 5.4˚ to 6˚ as the wavelength changes from 500 nm to 750 nm, while the average value of $\cos\Delta$ are around 0.92. The Ψ values of group-c1 cells are even smaller than the Ψ values of $10 \mu l / g$ LD treated cells since more LD medicine entered group-c1 cells. The $\cos\Delta$ values of group-c1 cells are only slightly smaller than the $\cos\Delta$ values of $10 \mu l / g$ LD treated cells since the morphology of cells in these two groups are similar.

The average Ψ spectra of group-c2 (including cells 24 to 28) increases from 6.6˚ to 7.3˚ as the wavelength changes from 500nm to 750nm, while the average value of $\cos\Delta$ are around 0.78. In group-c2 cells, trends of Ψ and $\cos\Delta$ are dramatically different from previous three groups of cells, due to the difference in morphology and damaged inner structure after LD medicine treatment.
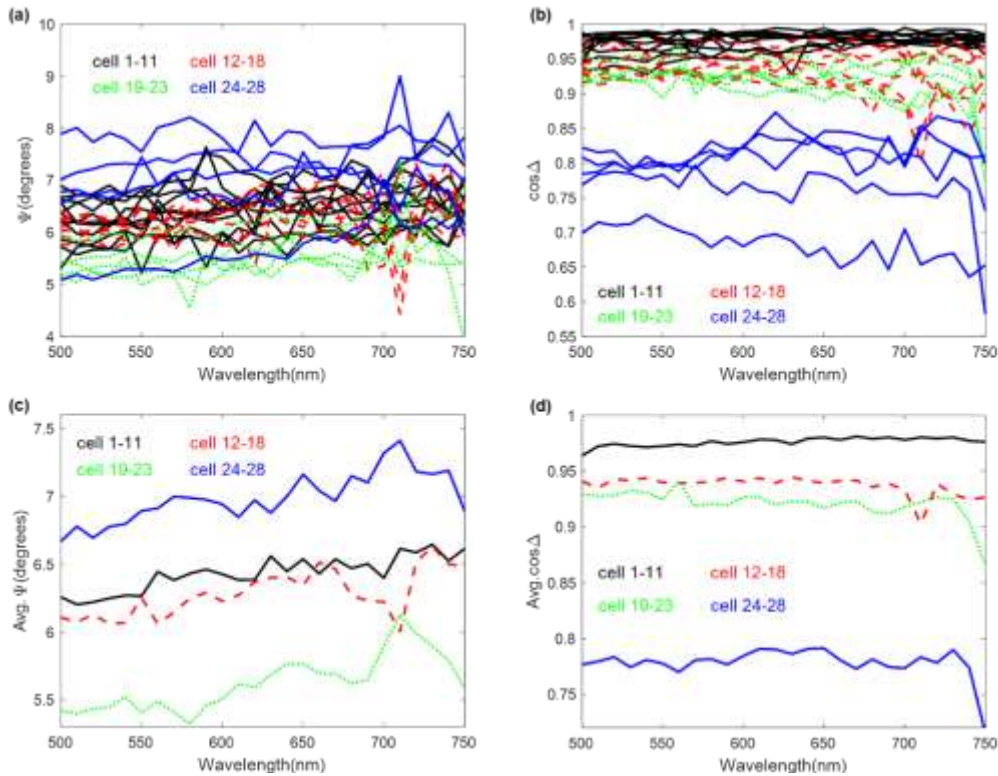
Figure 6. (a) Ψ spectra, (b) $\cos\Delta$ spectra of original colon cancer cells (cells 1-11), $10\mu l/g$ LD-treated colon cancer cells (cells 12-18), $50\mu l/g$ LD-treated colon cancer cells (group-c1: cells 19-23 and group-c2: cells 24-28).(c) Ψ spectra shown in (a) and (d) $\cos\Delta$ spectra shown in (b) averaged over cells within the same group.

3.2 MIE Images

We selected two most representative cells in each group for studying MIE images. Specular-reflection images for $[\tan\Psi, \sin\Delta, I_S, I_P]$ of original single colon cancer cells (cells 6 and 8), $10\mu l/g$ LD medicine treated single colon cancer cells (cells 13 and 17), $50\mu l/g$ LD medicine treated single colon cancer cells (cells 20 and 22) in group c1 and $50\mu l/g$ LD medicine treated single colon cancer cells (cells 25 and 28) in group c2 for three wavelengths (λ = 500nm,600nm, and 700nm) are shown in Fig. 7, 8, 9. The images for the shortest wavelength, λ = 500nm have better contrast than images for the other two wavelengthsand more sensitive to the morphology changes during drug treatment. For MIE images of original single colon cancer cells (cells 6 and 8), we observed clear ripple-like diffraction pattern surrounding each cell, which is related to the morphology of cell membrane, and several peaks inside the cell, which might be related to cavityresonancesof the dome-shaped cell [26].

For $10\mu l/g$ LD medicine treated single colon cancer cells (cells 13 and 17), the outer diffraction patterns in MIE images are enlarged, and stronger spikes appearnear the center.The size of cells 13 and 17 might be enlarged in comparison to cells 6 and 8,since more LD medicine enters these cells. For $50\mu l/g$ LD medicine treated single colon cancer cells (cells 20and 22) in group c1, the outer diffraction patterns in MIE images are further enlarged and the shape of cells appears elongated. The cavity resonance peaks become weaker due to the shape distortion.

For $50\mu l/g$ LD medicine treated single colon cancer cells (cells 25 and 28) in group-c2, the cavity resonance peaks disappear. Instead, some distributed scattering peaks appear, reflecting broken or expanded cellswith fractured nucleus. Since we do not expect to observe the cavity resonances of a broken cell, these distributed broken features are more likely due to light scattering from the small pieces of the fractured nucleus. We also noticed significant reduction in the magnitude of the diffraction ripples for cells 25 and 28 (in comparison to cells 20 and 22), which is attributed to the change of cell morphology from a smooth dome-shaped membrane to a wrinkled or broken membrane.

Figure 7. Specular-reflection images for original colon cancer cells and drug-treated colon cancer cells.The wavelength of incident light is 500nm. AOI≈60˚.
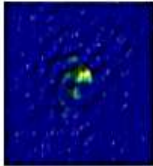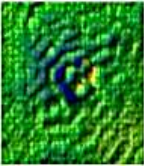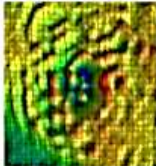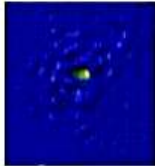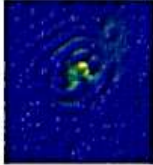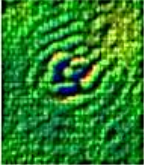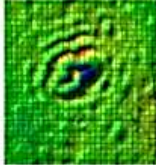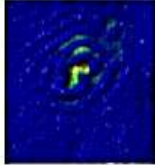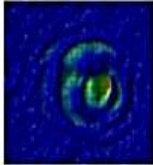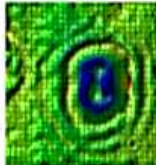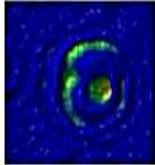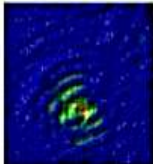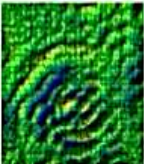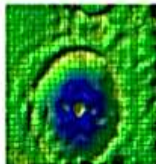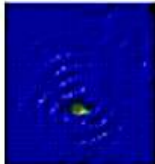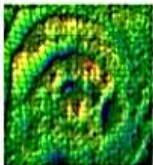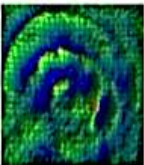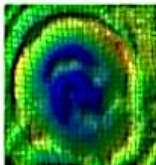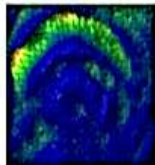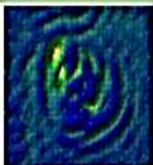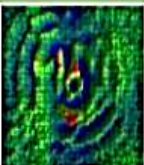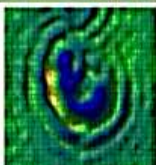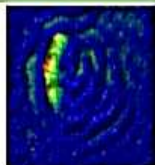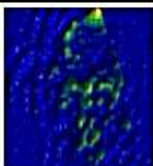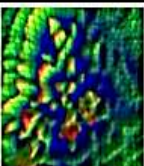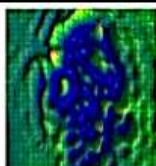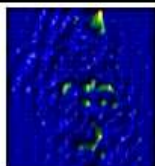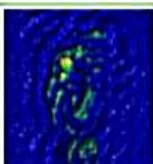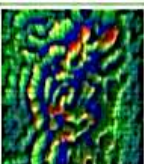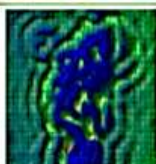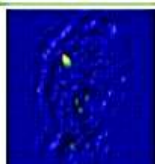
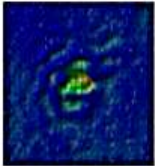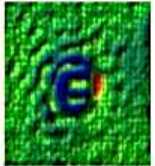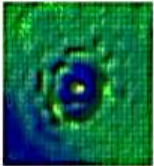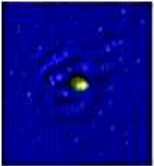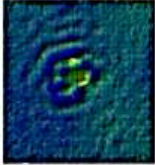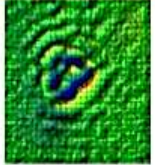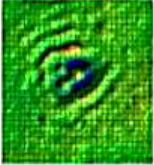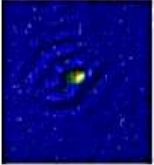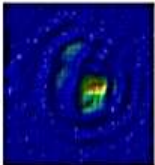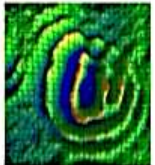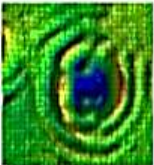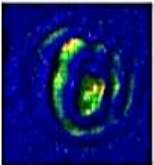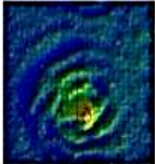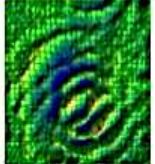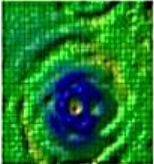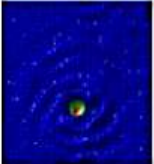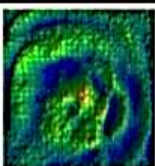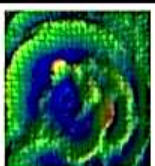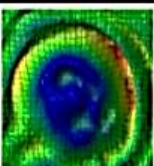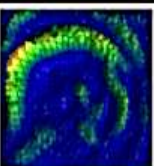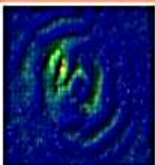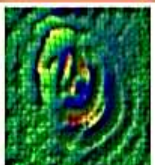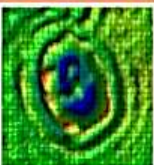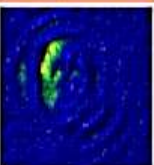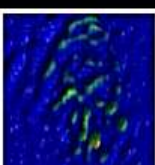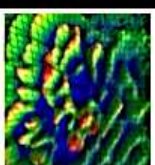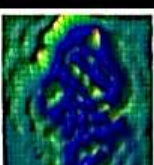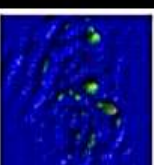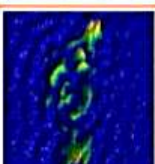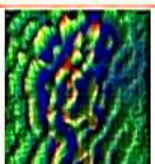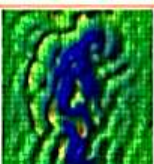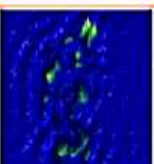| WL.=600nm	$\tan\psi$	$\sin\Delta$	Is	Ip
Original Cell 6				
Original Cell 8				
10ul/g LD treated Cell 13				
10ul/g LD treated Cell 17				
50ul/g LD Group-c1 Cell 20				
50ul/g LD Group-c1 Cell 22				
50ul/g LD Group-c2 Cell 25				
50ul/g LD Group-c2 Cell 28				

Figure 8. Specular-reflection images for original colon cancer cells and drug-treated colon cancer cells. The wavelength of incident light is 600nm. AOI≈60˚.
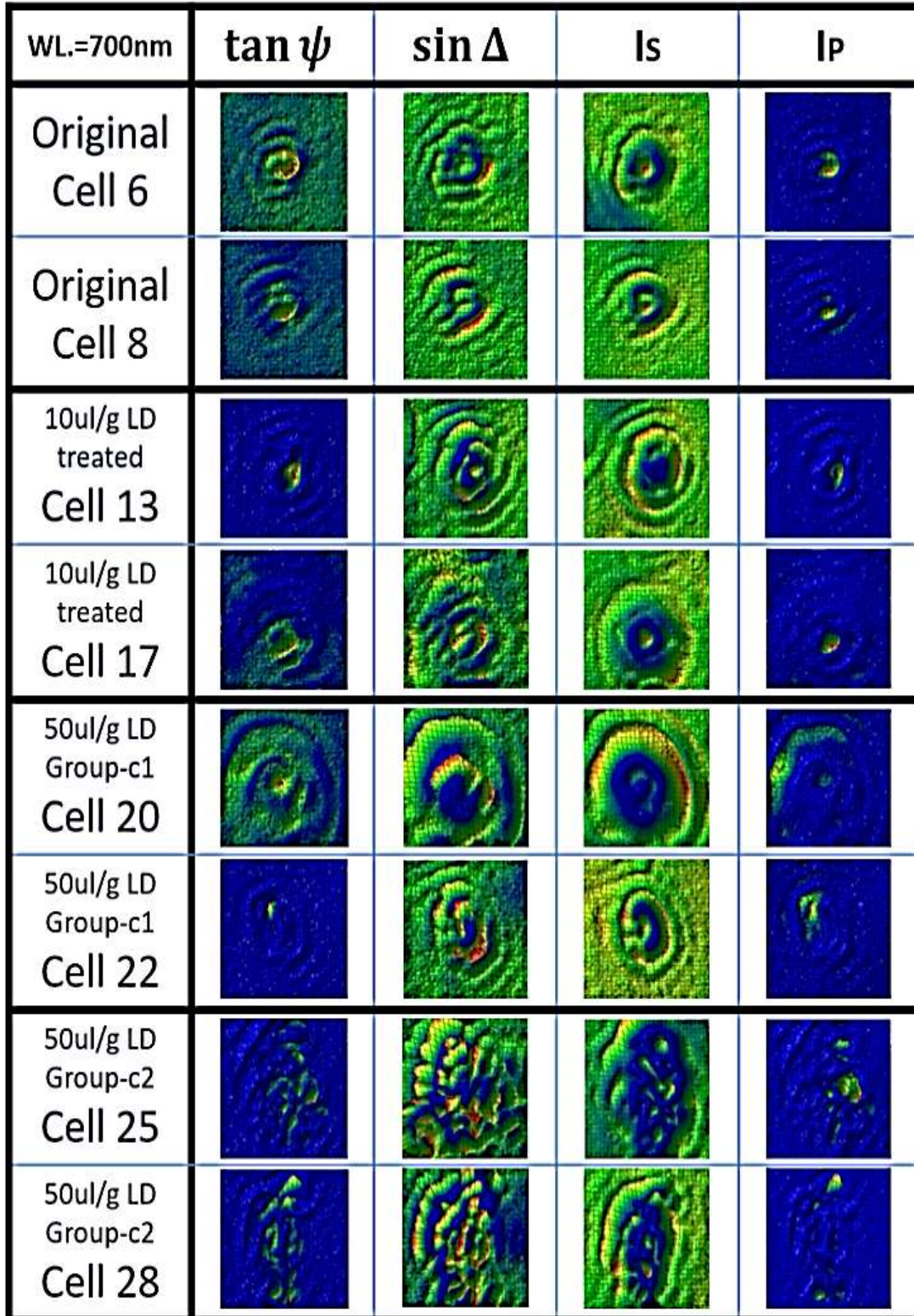
Figure 9. Specular-reflection images for original colon cancer cells and drug-treated colon cancer cells. The wavelength of incident light is 700nm. AOI≈60˚.

For in-depth analysis of the MIE images, we can separate them into three groups – the intensity related images (I_s, I_p), polarization-contrast related images ($\tan\Psi = |r_p/r_s|$), and phase related images ($\sin\Delta$). For intensity related images (I_s, I_p), the diffraction pattern outside the cell are clear in I_s but very faint in I_p. This is explained as follows. The measured ellintensity can be written as [26]:

$$I_\sigma(\mathbf{\rho}) = |E_\sigma^r + E_\sigma^s(\mathbf{\rho})|^2 = |E_\sigma^r|^2 + |E_\sigma^s(\mathbf{\rho})|^2 + 2\operatorname{Re}[E_\sigma^{r*} E_\sigma^s(\rho)] \text{ for } \sigma = s, p \quad \textbf{(12)}$$

where E_σ^r denotes the electric field due to direct reflection from the glass surface for the system without the cell and $E_\sigma^s(\mathbf{\rho})$ is the electric field due to scattering from the cell for the σ-polarization ($\sigma = s, p$).

In our case, we have $|E_\sigma^r|^2 \gg |E_\sigma^s(\mathbf{\rho})|^2$ for $\sigma = s$. Thus, the I_S image is essentially given by the last term (the cross term) in Eq. (12) plus a constant background due to $|E_s^r|^2$. For the p-polarization, we have $|E_p^r|^2 \approx 0$ for AOI near the Brewster angle. Thus, the I_p image is mainly due to the intensity of scattered light from the cell, which is $|E_p^s(\mathbf{\rho})|^2$ and is much weaker than I_s. Furthermore, I_s is proportional to the $E_s^s(\rho)$ (first order), while I_p is proportional to $|E_p^s(\mathbf{\rho})|^2$ (second order). Thus the peak structures in the I_p image should appear narrower (but weaker) in comparison to similar peaks in the I_s image.

The polarization-contrast related images ($\tan\Psi$) provide a means to remove some noise caused by the stray light, scattered light from dust on the substrate, or non-uniform distribution of light intensity, since these effects canbe cancelled out when we take difference or ratio of r_s and r_p. Thus, it has potential to observe more faithful signal related to light scattered from the object of interest. Here, we noticed that the $\tan\Psi$ image reveals more structures inside the cell. So, the $\tan\Psi$ images could give more information regarding the nucleus of the cell.

The $\sin\Delta$ imagescan reveal the phase information which is sensitive to the morphology of cells. Comparing the phase related images with the intensity related images, we noticed that the structure features in the phase related images are like the gradient of the spatial distribution of intensity related images. Thus, $\sin\Delta$ images are more sensitive to sharp structure change near the boundary of objects.The sharp ring structures in $\sin\Delta$ images reveal the boundaries of cells.

IV. CONCLUSION

In this study, LD medicine treatment on fusiform single colon cancer cells were observed by microscopic imaging ellipsometry (MIE) with a modified Multiskop setup. We introduced some MIE parameters ($\tan\Psi$, $\sin\Delta$, I_s, I_p) which have simple physical meanings and provide complementary information regarding the polarization-dependent intensities, the polarization contrast, and phase difference of reflectivities for s- and p-polarized light. For specular-reflection mode, $\tan\Psi$ and $\sin\Delta$ images provide useful information for polarization contrast and phase difference. Ψ and $\cos\Delta$ spectra in visible wavelength range (500nm-750nm) shows significant difference for drug treated single colon cancer cells and untreated original single colon cancer cells. Specular MIEimages in wavelengths (500nm, 600nm, and 700nm) can reveal the morphology of fusiform single colon cancer cells (when they are untreated) by examining the diffraction patterns of light scattering from the membrane. These patterns became expanded or irregular for LD medicine-treated cells, indicating the distortion or fracturing of the cell membrane. For specular mode, we observed cavity-resonance relateddiffraction peaks for untreated cells and multiple peaks related to light scattering from the fractured nucleus for treated cells. Therefore, we demonstrates the usefulness of MIE for studying the drug treatment on cancer cells via analysis of the set of MIE parameters ($\tan\Psi$, $\sin\Delta$, I_s, I_p). More quantitative information can be obtained when compared with computer simulation of the light scattering image pattern of a cell with some surmised morphology, which will be left for future studies. This technique introduced here should be useful for future biomedical research on other biological systems.

ACKNOWLEDGEMENTS

REFERENCES

[1]. Kherlopian, A R; Song, T; Duan, Q; Neimark, M A; Po, M J; Gohagan, J K; and Laine, A F, 2008, "A Review of Imaging Techniques for Systems Biology," Bmc. Syst. Biol. 2 74

[2]. Neil, M A A;Juskaitis, R; and Wilson, T, 1997,"Method of Obtaining Optical Sectioning by Using Structured Light in a Conventional Microscope,"Opt. Lett. 22 1905-1907

[3]. de Jonge, N; and Ross, F M, 2011,"Electron Microscopy of Specimens in Liquid,"Nat. Nanotechnol. 6 695-704

[4]. Hansma, P K; Cleveland, J P;Radmacher, M; Walters, D A;Hillner, P E;Bezanilla, M; Fritz, M; Vie, D; and Hansma, H G, 1994,"Tapping Mode Atomic-Force Microscopy in Liquid,"Appl. Phys. Lett. 64 2454-2456

[5]. Ling, D; Hackett, M J; and Hyeon, T, 2014,"Cancer Imaging Lighting up Tumours,"Nat. Mater. 13 122-124

[6]. Frangioni, J V, 2008,"New Technologies for Human Cancer Imaging,"J. Clin. Oncol. 26 4012-4021

[7]. Gabriel, M;Decristoforo, C;Kendler, D;Dobrozemsky, G;Heute, D;Uprimny, C; Kovacs, P;Guggenberg, E V; Bale, R; and Virgolini, I J, 2007,"68Ga-DOTA-Tyr3-octreotide PET in Neuroendocrine Tumors: Comparison with Somatostatin Receptor Scintigraphy and CT,"J. Nucl. Med. 48 508-518

[8]. Golman, K;Lerche, M;Pehrson, R; and Ardenkjaer-Larsen, J H, 2006,"Metabolic Imaging by Hyperpolarized 13C Magnetic Resonance Imaging for In Vivo TumorDiagnosis," Cancer Res. 66 10855-10860

[9]. Jonischkeit, T;Bommerich, U;Stadler, J; and Woelk, K, 2006,"Generating Long-Lasting 1H and 13C Hyperpolarization in Small Molecules with Parahydrogen-Induced Polarization,"J. Chem. Phys. 124 201109

[10]. Park, J-H; Cho, H-J; Yoon, H Y; Yoon, I-S; Ko, S-H; Shim, J-S; Cho, J-H; Park, J H; Kim, K; Kwon, I C; and Kim, D-D, 2014,"Hyaluronic Acid Derivative-Coated NanohybridLiposomes for Cancer Imaging and Drug Delivery,"J. Control. Release 174 98-108

[11]. Jokerst, J V; Cole, A J; Van de Sompel, D; and Gambhir, S S, 2012, "Gold Nanorods for Ovarian Cancer Detection with Photoacoustic Imaging and Resection Guidance via Raman Imaging in Living Mice,"ACS nano 6 10366-10377

[12]. Wu, X; Wu, M; and Zhao, J X, 2014,"Recent Development of Silica Nanoparticles as Delivery Vectors for Cancer Imaging and Therapy,"Nanomed.-Nanotechnol. 10 297-312

[13]. Passaglia, E; Stromberg, R R; and Kruger, J,1964,"Ellipsometry in the Measurement of Surfaces and Thin Films,"Symposium Proceedings 256

[14]. Holmes, D A, 1967,"On the Calculation of Thin Film Refractive Index and Thickness by Ellipsometry,"Appl. Opt. 6 168-169

[15]. Aspnes, D E; and Theeten, J B, 1979, "Investigation of Effective-Medium Models of Microscopic Surface-Roughness by Spectroscopic Ellipsometry,"Phys. Rev. B 20 3292-3302

[16]. Lucovsky, G; and Mantini, M J, 1987,"Low-Temperature Growth of Silicon Dioxide Films - a Study of Chemical Bonding by Ellipsometry and Infrared-Spectroscopy,"J. Vac. Sci. Technol. B 5 530-537

[17]. Meera, V; and Setlur, G S, 2010,"Ellipsometry of Graphene on a Substrate,"J. Appl. Phys. 107

[18]. Yim, C; O'Brien, M; McEvoy, N; Winters, S; Mirza, I; Lunney, J G; and Duesberg, G S, 2014,"Investigation of the Optical Properties of MoS2 Thin Films Using Spectroscopic Ellipsometry," Appl. Phys. Lett. 104 103114

[19]. Note that we have adopted the notation in physics community, which leads to a flip of sign in Δ in comparison to the notation used in optics community.

[20]. Qi, C; Lin, Y; Feng, J; Wang, Z-H; Zhu, C-F;Meng, Y-H; Yan, X-Y; Wan, L-J; and Jin, G, 2009,"Phage M13KO7 Detection with Biosensor Based on Imaging Ellipsometry and AFM Microscopic Confirmation,"Virus Res. 140 79-84

[21]. Jin, G; Meng, Y H; Liu, L; Niu, Y; Chen, S; Cai, Q; and Jiang, T J, 2011,"Development of Biosensor Based on Imaging Ellipsometry and Biomedical Applications,"Thin Solid Films 519 2750-2757

[22]. Munteanu, S; Garraud, N; Roger, J P; Amiot, F; Shi, J; Chen, Y; Combellas, C; and Kanoufi, F, 2013,"In Situ, Real Time Monitoring of Surface Transformation: Ellipsometric Microscopy Imaging of Electrografting at Microstructured Gold Surfaces,"Analytical Chemistry 85 1965-1971

[23]. Wu, C H; Kuo, Y H; Hong, R L; and Wu, H C, 2015,"α-Enolase-binding peptide enhances drug delivery efficiency and therapeutic efficacy against colorectal cancer,"Science Translational Medicine 7, 290ra91, 1-14

[24]. Fan, J-Y; Li, H-X; and Wu, F-Q, 2003,"A Study on Transmitted Intensity of Disturbance for Air-Spaced Glan-Type Polarizing Prisms,"Optics Communications 223 11–16

[25]. Chen, Y-D; Hsu, H Y; Khaleel, M I; Chang, Y-C; Wu, C-H; and Wu, H-C, 2016,"Study of Biological Reaction in Cancer Cell with Spectroscopic Imaging Ellipsometry,"Proceedings of SPIE Conference on Optics+Photonics 992505-992513

[26]. Chang, Y-C; Xie, H-Y; Hsiao, A F-C; Chen, Y-D; and Ngo, T H B, 2016,"Optical Sensing of Nanoscale Objects via Computation-Aided Microscopic Imaging Ellipsometry,"Sci. Lett. J. 5 229